Multicomponent topology optimization method considering assemblability using a fictitious physical model

R. Hirosawa[a], M. Noda[b], K. Matsushima[b,*], Y. Noguchi[c], T. Yamada[c]

[a]*Department of Mechanical Engineering, School of Engineering, The University of Tokyo.*
[b]*Department of Mechanical Engineering, Graduate School of Engineering, The University of Tokyo.*
[c]*Department of Strategic Studies, Institute of Engineering Innovation, Graduate School of Engineering, The University of Tokyo.*

Abstract

This paper proposes a multicomponent topology optimization method that considers assemblability. Generally, it is difficult to consider assemblability in topology optimization; however, in this study, we achieve it by introducing a fictitious physical model. To perform multicomponent topology optimization, the extended level set method is used to represent multiple components. First, the assembly constraints are formulated using a fictitious physical model limited to two components. Then, by considering stepwise assembly, the constraint is extended to three or more components. In addition, topology optimization algorithms are constructed using the finite element method. Several numerical examples demonstrate that the proposed method can obtain structures with assemblability and has low initial structure dependence.

Keywords: Topology optimization, Assemblability, Extended level set method, Multicomponent design, Fictitious physical model, Finite element method, FreeFEM

1. Introduction

Topology optimization methods are used to create and design the optimal shape of structures based on mathematical and physical evidence, and topology optimization is attracting increasing attention as it provides the highest degree of design freedom among structural optimization methods because it permits topology changes. Topology optimization was initially proposed by Bendsøe and Kikuchi [1]. Since then, several topology optimization methods have been developed, e.g., the density method [2, 3], the homogenized design method [4, 5], and the level set method [6–9]. Recently, it has been reported that these methods have been applied to a wide range of design problems, e.g., the vibration problem [10, 11], heat conduction problems [12–14], electromagnetic problems [15, 16], and acoustic problems [17, 18]. Topology optimization has also been employed in the design phase of industrial products. Examples include the design optimization of material reinforcement to improve automobile body rigidity [19] and the structural performance

*Corresponding author
Email address: matsushima@mech.t.u-tokyo.ac.jp (K. Matsushima)

and stability enhancement of a commercial aircraft vertical stabilizer component [20]. However, topology optimization is essentially a method to design the shape of a single device or component; thus, it cannot be used to comprehensively design an entire mechanical structure.

Therefore, in this study, we attempt to realize such a design. First, we propose a structural optimization method that considers assemblability. One way to achieve assemblability in topology optimization is the uniform cross-section surface constraint [8, 21] in the level set-based topology optimization. The reaction–diffusion equation is commonly used to update the level set function in level set-based topology optimization. In the reaction–diffusion equation, the coefficients of the diffusion term can be extended to a second-order tensor, and equal-section constraints can be imposed by setting the component corresponding to a certain direction to be sufficiently large. This is expected to result in a shape that can be assembled; however, it can be excessive as a constraint and may not result in a high-performance structure. In topology optimization methods, manufacturability and assemblability are often formulated based on cavity exclusion constraints [22–27] and optimization of a joint distribution [28]; however, these approaches are not always sufficient to ensure assemblability. Assemblability can also be achieved using heuristic or nongradient approaches. For example, Luo et al. [29] proposed a framework to partition 3D objects in additive manufacturing based on binary space partitioning. In addition, Attene [30] introduced a heuristics algorithm for disassembly and packing of 3D objects. Zhou et al. [31] and Guirguis et al. [32] presented multicomponent topology optimization methods based on a genetic algorithm. Genetic algorithms have also been used in part decomposition techniques in additive manufacturing processes [33–36]. However, gradient-based approaches are preferable from a computational perspective because multicomponent optimization requires a large number of design variables. In the proposed method, geometric constraints are represented implicitly using a fictitious physical model, which allows constraint violation during the optimization process, and this result in geometric constraints with low initial structure dependency.

One advantage of having assemblability in mechanical structures is the ease of designing with multiple materials. Recently, in the design of mechanical structures, increasing attention is being paid to design methods that organically combine multiple materials with different properties. By combining multiple materials, seemingly contradictory properties, e.g., high strength and low weight, can be achieved simultaneously. It has been reported that some structural designs, e.g., negative thermal expansion, can only be realized using multiple materials [37]. The multimaterial level set (MMLS) method [38] and vector valued level set (VVLS) method [39] are two examples of multimaterial representations based on level set methods. The MMLS method is characterized by an asymmetric technique for defining materials, which makes it more dependent on the initial structure, and this effect becomes increasingly apparent when the number of material types increases. The VVLS method is characterized by its symmetric material representation and low dependence on the initial structure. However, it has asymmetry at the interface that divides the level set function space, which affects regularization. The extended level set (X-LS) method [40] eliminates the

asymmetry in the VVLS method and achieves complete symmetry in the material definition.

In this study, we use the extended level set (X-LS) method and propose a topology optimization method that considers multiple components and assemblability.

The remainder of this paper is organized as follows. In Section 2, we outline topology optimization based on the X-LS method, and in Section 3, we formulate the assembly constraints based on a fictitious physical model. In Section 4, we formulate the mean compliance minimization problem considering the assembly constraints. In Section 5, we describe the optimization algorithm and a concrete numerical implementation method. In Section 6, we present a numerical analysis example to confirm the validity and effectiveness of the proposed method. Finally, conclusions are given in Section 7. Note that a detailed derivation of the topological derivatives is presented in the Appendix for a fictitious physical model.

2. Extended level set-based topology optimization

Here, we describe topology optimization based on the X-LS method used in this study.

2.1. Level set method

Before explaining the X-LS method, we first explain the conventional level set method.

The topology optimization problem uses the following characteristic function χ to represent the object region Ω to be designed.

$$\chi = \begin{cases} 1 & \text{for} \quad \boldsymbol{x} \in \Omega \\ 0 & \text{for} \quad \boldsymbol{x} \in D \backslash \Omega. \end{cases} \tag{1}$$

However, this characteristic function can be changed in infinitesimal intervals; thus, the topology optimization problem with characteristic function χ as a design variable is an ill-posed problem. Therefore, based on regularization, the level set-based topology optimization method [8] forms this as a well-posed problem. In this method, the shape of the structure to be designed is represented by the isosurface of a scalar function called the level set function, and regularization can be achieved by determining the smoothness of the level set function appropriately.

In the level set method, the characteristic function χ_ϕ is defined as follows using the level set function ϕ:

$$\chi_\phi = \begin{cases} 1 & \text{for} \quad \phi(x) \geq 0 \\ 0 & \text{for} \quad \phi(x) < 0. \end{cases} \tag{2}$$

In this method, the optimization problem is formulated with the level set function $\phi(x)$ as the design variable. Next, we describe how the level set function is updated. In level set-based topology optimization [8], a virtual time t is introduced, and the topology optimization problem is replaced by a time evolution

problem for ϕ to update the level set function based on the reaction–diffusion equation as follows:

$$\frac{\partial \phi}{\partial t} = -K(D_T J - \tau \nabla^2 \phi), \tag{3}$$

where $K > 0$ is a proportionality constant, $D_T J$ is the topological derivative, and $\tau > 0$ is a regularization parameter. Here, the topological derivative $D_T J$ is the ratio of the variation of the objective function J to the volume or area of the small region Ω_ε when a small region $\Omega_\varepsilon > 0$ is inserted into the structure represented by region Ω. $D_T J$ is defined as follows:

$$D_T J(x_0) = \lim_{\varepsilon \to 0} \frac{J(\varepsilon) - J(0)}{f(\varepsilon)}. \tag{4}$$

Here, x_0 is the central coordinate of Ω_ε, and $f(\varepsilon)$ is a function that depends on ε and is defined such that the above limit exists.

2.2. Extended level set method

In the following, we briefly describe the X-LS method [40], which extends the level set method described above to multiple materials.

In the X-LS method, the X-LS function $\phi_{ij}(\boldsymbol{x})$ defined in the real space $\mathbb{R}^d$ (where d is the dimension of the problem) is employed rather than the conventional level set function. Figure 1 shows a conceptual diagram of the X-LS method.

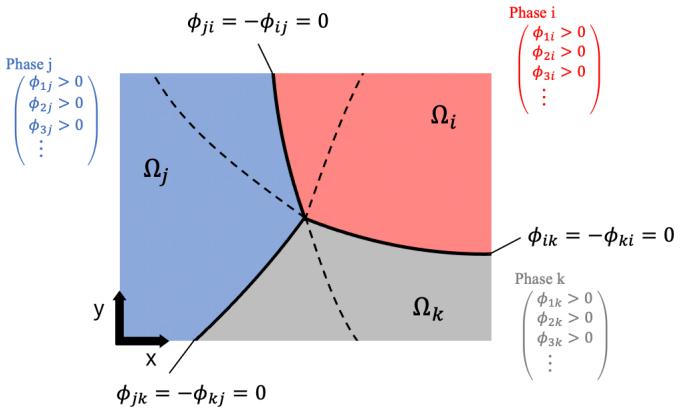

Figure 1: Concept of X-LS method. Material domains and X-LS functions.

The X-LS function $\phi_{ij}(i \neq j)$ and the domain of each material i, j correspond as follows:

$$\begin{cases} \phi_{ij}(\boldsymbol{x}) > 0 & \text{if } \boldsymbol{x} \in \Omega_i \\ \phi_{ij}(\boldsymbol{x}) = 0 & \text{if } \boldsymbol{x} \in \Gamma_{ij} \\ \phi_{ij}(\boldsymbol{x}) < 0 & \text{if } \boldsymbol{x} \in \Omega_j, \end{cases} \tag{5}$$

where Ω_i, Ω_j are the regions occupied by materials i, j, respectively, and Γ_{ij} is their boundary. To satisfy the symmetry in Eq. (5), we assume that the X-LS function satisfies the following equality:

$$\phi_{ij} = -\phi_{ji}. \tag{6}$$

Here, the characteristic function χ_m, which indicates the region of the mth phase, is defined as follows:

$$\chi_m(\boldsymbol{x}) = \begin{cases} 1 & \text{if} \quad \boldsymbol{x} \in \Omega_m \\ 0 & \text{if} \quad \boldsymbol{x} \in D \backslash \Omega_m, \end{cases} \tag{7}$$

where Ω_m denotes the region of the mth phase. In the X-LS method, the characteristic function of the mth phase χ_m is expressed using the X-LS function ϕ_{ij} as follows:

$$\chi_m(\boldsymbol{x}) = \prod_{i \neq m} H(\phi_{im}), \tag{8}$$

where $H(s)$ is a Heaviside function:

$$H(s) = \begin{cases} 1 & \text{if} \quad s \geq 0 \\ 0 & \text{if} \quad s \leq 0. \end{cases} \tag{9}$$

As can be seen from the Equation (6), there are $M(M-1)/2$ independent components in the X-LS function. In addition, one of the M phases should be assigned to each coordinate $\boldsymbol{x}$; thus, the X-LS function satisfies the following.

$$\sum_m \chi_m(\phi_{im}) = 1. \tag{10}$$

Next, we discuss the update of the X-LS function. In the X-LS method, as in the level set method described in Section 2.1, the X-LS function is updated as a time evolution problem expressed by the following reaction–diffusion equation:

$$\frac{\partial \phi_{ij}}{\partial t} = -K(D^{ij}J - \tau_{ij}\nabla^2 \phi_{ij}), \tag{11}$$

where t is a virtual time, $K > 0$ is a constant, τ_{ij} is a coefficient for regularization, and $D^{ij}J$ is an extended topological derivative (expressed using the conventional topological derivative $D_T^{ij}J$), which is defined as follows:

$$D^{ij}J = D_T^{kj}J - D_T^{ki}J, \tag{12}$$

where the topological derivative $D_T^{ij}J$ is the ratio of the variation of the objective function to the volume or area of the small region when a small region of material j and radius $\varepsilon > 0$ is inserted into the region of material i. Note that the extended topological derivatives is explained in detail in Section 4.2.

3. Formulation of assembly constraints using fictitious physical models

Here, we formulate geometric constraints that consider assemblability in consideration of multiple components.

We attempt to manufacture multiple components separately and assemble them to form a single structure. However, evaluating the assemblability of separately manufactured components is very difficult due to the positional relationship and interference with other components. In addition, it is even more difficult to optimize an assembled whole structure simultaneously.

Therefore, we focus on the fact that the assemblability of a structure can be attributed to decomposability, which means that a structure can be decomposed into multiple components by following the assembly procedure in reverse. If we seek to evaluate decomposability, we only need to consider a single structure, i.e., the entire structure. Thus, decomposability can be easily incorporated into optimization of the entire structure. Therefore, in this study, the assembly constraint is realized by evaluating the decomposability of the entire structure obtained by the optimization calculation.

3.1. Geometrical requirements

First, we clarify the geometric requirements of decomposing a single component from an entire structure comprising multiple components. Here, there are two primary shapes that are problematic in disassembly. The first is called an undercut shape, which is a convex or concave shape that gets stuck when disassembling. The second is an interior void shape in which other components are inserted into the structure and cannot be removed. Examples of these two shapes are shown in Figure 2. If one of these shapes is included in the overall structure, it cannot be disassembled. In other words, the assembly constraint is a geometric constraint that excludes undercut and interior void shapes.

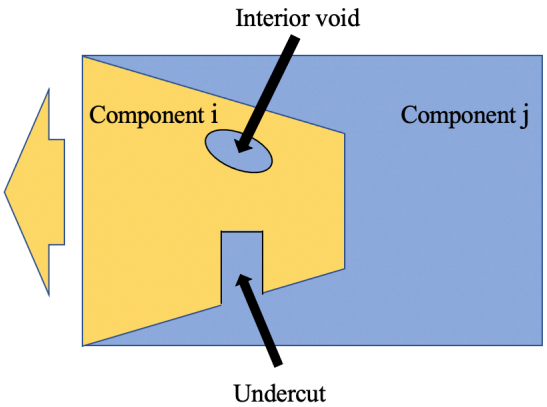

Figure 2: Undercut and interior void geometry.

3.2. Fictitious physical model

If the designed structure is simple, it is easy to determine whether each component can be disassembled; however, for a more complex structure, it may be difficult to evaluate its decomposability. In design processes that use structural optimization methods, designers must analyze the decomposability of the obtained structure and modify it in consideration of both structural optimization and decomposability. This requires extensive knowledge, design experience, and trial and error. Thus, to solve this problem, we propose a method to evaluate geometric features implicitly using a fictitious physical model technique [41, 42].

Here, to eliminate shapes that do not satisfy decomposability, we must consider a physical model that has some value only in object regions that include undercut or interior void shapes. First, we must consider the region through which a part passes when it is decomposed. For example, Figure 3 shows the region through which component i in Figure 2 passes when it is disassembled to the left. This passthrough region can be expressed as a shadow of component i when fictitious light is illuminated from the right. This shadow region is shown in Figure 4. Similarly, we can express such a passthrough region by considering a fictitious heat flow [42] in the same direction as the decomposition direction. In this study, for the ease of numerical analysis, the fictitious heat field is introduced to represent the passage region.

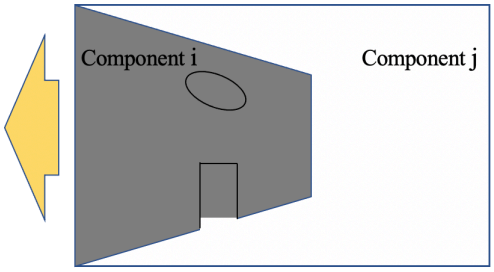

Figure 3: Passthrough area of component i.

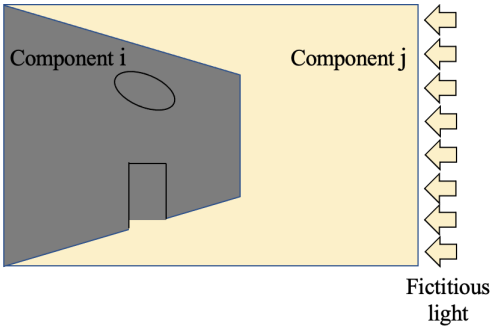

Figure 4: Shadow area of component i.

For simplicity, we explain the introduction of a fictitious heat field ψ using a case with two components. Here, assume that component i is decomposed from a structure comprising components i and j to the specified direction $\boldsymbol{d}_i$ (left side), as shown in Figure 2. In this case, we consider fictitious internal heat generation in the region of component i. Note that the amount of heat generated is proportional to the difference between 1 and the heat value $\psi_i(\boldsymbol{x})$ at that point, i.e., $(1 - \psi_i(\boldsymbol{x}))$. Here, it is assumed that the entire analysis region is filled with an anisotropic material having high thermal conductivity in the specified direction $\boldsymbol{d}_i$. Considering a fictitious heat flow along the prescribed direction $\boldsymbol{d}_i$ from the boundary Γ_{in} on the right side of the analysis domain, we obtain a fictitious temperature distribution (Figure 5) in the steady state, i.e., a distribution where the temperature is $\psi_i = 1$ downstream of component i and $\psi_i = 0$ in the rest of the domain. Therefore, by extracting only the region of component j from the high-temperature region

where $\psi_i = 1$, we can obtain a model that has large values only in regions that include undercut or interior void shapes, as shown in Figure 6.

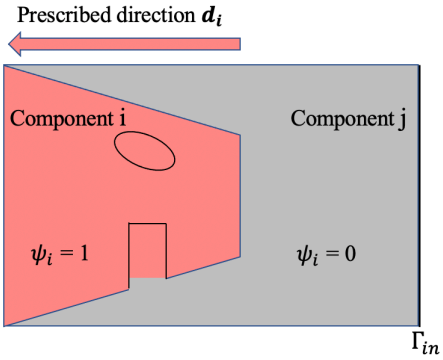

Figure 5: Fictitious heat field ψ_i.

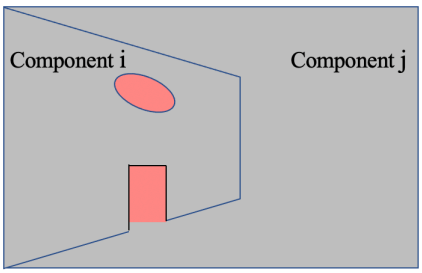

Figure 6: High-temperature domains in component j.

The high-temperature region and component j, i.e., the region where $\psi_i \chi_j$ has a large value, is where the assembly constraint is violated. Here, χ_j is a characteristic function that takes a value of 1 in the region of component j and 0 in other regions. Thus, we can exclude undercut and interior void shapes and impose constraints on the decomposition of component i by minimizing the following functional:

$$F_j = \int_D \psi_i \chi_j \, d\Omega. \tag{13}$$

Note that the subscript of F_j is j because Equation (13) is a constraint function for the region of component j. ψ_i is a fictitious heat field where heat is generated in the region of component i and flows in the specified direction $\boldsymbol{d}_i$. ψ_i is obtained by solving the following steady advection–diffusion equation.

$$\begin{cases} -L^2 \mathrm{div}(\boldsymbol{A}_i \cdot \nabla \psi_i) + LV \boldsymbol{d}_i \cdot \nabla \psi_i = \beta \chi_i (1 - \psi_i) & in\ D \\ \psi_i = 0 & on\ \Gamma_{\mathrm{in}} \\ \boldsymbol{n}_i \cdot \nabla \psi_i = 0 & on\ \partial D \backslash \Gamma_{\mathrm{in}}, \end{cases} \tag{14}$$

where $\boldsymbol{A}_i$ is the diffusion coefficient tensor, β is a parameter representing the degree of internal heating of the object region, L is the representative length for dimensionlessness, $\boldsymbol{n}_i$ is the outward unit normal vector, and V is the velocity of advection. Here, the diffusion coefficient tensor sets the prescribed direction component to be greater than the other components, i.e., $\boldsymbol{A}_i$ is expressed as follows:

$$\boldsymbol{A}_i = \boldsymbol{d}_i \otimes \boldsymbol{d}_i + \varepsilon \sum_{m=1}^{N-1} \boldsymbol{e}_m \otimes \boldsymbol{e}_m, \tag{15}$$

where N is the space dimension, $\boldsymbol{e}_m$ denotes the orthonormal basis in the orthonormal complementary space of $\boldsymbol{d}$, and $\varepsilon > 0$ is a tiny constant.

In the two-component case, decomposing component i to the left is equivalent to decomposing component j in the opposite direction (i.e., to the right). Thus, the decomposability of component i is also satisfied by considering the heat field ψ_j generated from component j that flows in the direction $\boldsymbol{d}_j(=-\boldsymbol{d}_i)$, as shown in Figure 7, and excluding the region in Figure 8 represented by $\psi_j\chi_i$. In this case, the constraint function for component i is expressed as follows:

$$F_i = \int_D \psi_j \chi_i \, d\Omega. \tag{16}$$

Therefore, to consider the symmetry of components i and j, we define a new constraint function, i.e., the product of two constraint functions, as a constraint function on decomposition of components i and j as follows:

$$J_{ij} = F_i \cdot F_j \tag{17}$$

$$= \int_D \psi_j \chi_i \, d\Omega \cdot \int_D \psi_i \chi_j \, d\Omega. \tag{18}$$

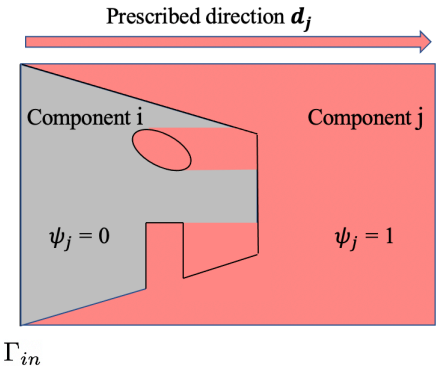

Figure 7: Fictitious heat field ψ_j.

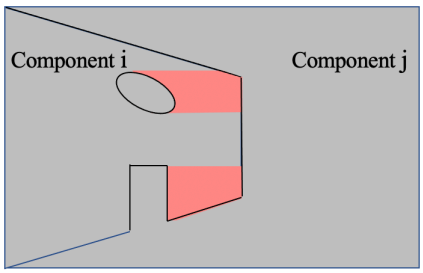

Figure 8: High-temperature domains in component i.

3.3. Application to three or more components

The case of three or more components can also be attributed to the two-component case by considering stepwise decomposition. As an example, we discuss the case of four components (indexed by k, l, m, n). Here, assume that we first decompose component k to the left (Step 1), then decompose component l to the right (Step 2), and finally decompose components m and n up and down (Step 3).

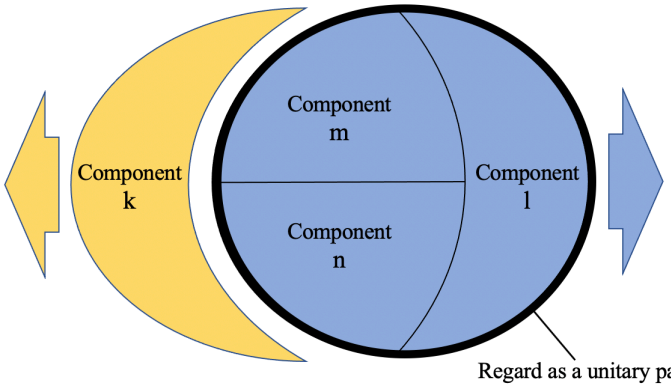

Figure 9: Step 1.

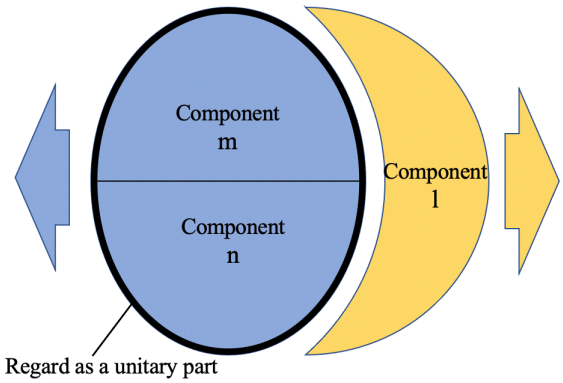

Figure 10: Step 2.

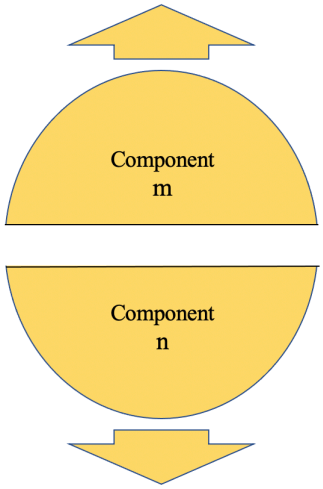

Figure 11: Step 3.

When component k is decomposed to the left, the same constraint function used in the two-component case can be defined by treating the remaining components l, m, n as a single component (Figure 9). In this case, the constraint function can be expressed as follows:

$$J_{k \cdot lmn} = F_k \cdot F_{lmn} \tag{19}$$

$$= \int_D \psi_{lmn} \chi_k \, d\Omega \cdot \int_D \psi_k \chi_{lmn} \, d\Omega, \tag{20}$$

where χ_{lmn} is the characteristic function that represents the area of the combined components l, m, n, and ψ_{lmn} is the heat field generated from χ_{lmn} that flows to the right. Next, when decomposing component l to the right, we treat the remaining components m, n as a single component (Figure 10) and define the

constraint function as follows:

$$J_{l\cdot mn} = F_l \cdot F_{mn} \tag{21}$$

$$= \int_D \psi_{mn}\chi_l \, d\Omega \cdot \int_D \psi_l \chi_{mn} \, d\Omega, \tag{22}$$

where χ_{mn} is the characteristic function that represents the region of the combined components m, n, and ψ_{mn} is the heat field heated from χ_{mn} that flows to the left. Finally, when components m, n are decomposed into upper and lower parts (Figure 11), the constraint function is expressed as follows:

$$J_{m\cdot n} = F_m \cdot F_n \tag{23}$$

$$= \int_D \psi_n \chi_m \, d\Omega \cdot \int_D \psi_m \chi_n \, d\Omega. \tag{24}$$

Optimization to a structure in which these four components can be assembled in stages can be achieved by minimizing the constraint function $\tilde{J}$, which is the sum of the constraint functions $J_{k\cdot lmn}$, $J_{l\cdot mn}$, and $J_{m\cdot n}$ corresponding to the above three stages of decomposition as follows:

$$\tilde{J} = J_{k\cdot lmn} + J_{l\cdot mn} + J_{m\cdot n}.. \tag{25}$$

4. Formulation of optimization problems

The above assembly constraints can be easily incorporated into structural optimization to obtain an optimal structure that achieves high performance with multicomponent assemblability. Here, we first formulate the optimization problem, and then we derive the design sensitivity to the optimization problem.

4.1. Application to optimization problems

Assume a surface force $\boldsymbol{t}$ is acting on boundary Γ_t of an isotropic linear elastic body Ω fixed at boundary Γ_u. Here, the displacement field is denoted $\boldsymbol{u}$, the elastic tensor is denoted $\boldsymbol{C}$, and the small strain tensor is denoted $\boldsymbol{\epsilon}(\boldsymbol{u}) = (\boldsymbol{\nabla u} + \boldsymbol{\nabla u}^T)/2$. The mean compliance minimization problem for m components with assembly constraints is formulated as follows:

$$\inf_{\phi_{ij}} \int_{\Gamma_t} \boldsymbol{t} \cdot \boldsymbol{u} \, d\Gamma \tag{26}$$

subject to :

$$\tilde{J} = 0 \tag{27}$$

$$E = \int_{\Gamma_t} \boldsymbol{t} \cdot \boldsymbol{u} \, d\Gamma - \int_D \epsilon(u) : \boldsymbol{C} : \epsilon(\tilde{u}) \, d\Omega = 0 \tag{28}$$

$$\frac{\int_D \chi_i d\Omega}{\int_D d\Omega} - V_i^{max} \leq 0 \qquad \text{i} = 1, 2, ..., \text{m}, \tag{29}$$

where $\tilde{J}$ is the constraint function of the assembly constraint defined in Equation (25), and $V_i^{\max}$ is the maximum percentage of the material area that component i can occupy.

4.2. Sensitivity analysis

In the following, we derive the extended topological derivatives for the assembly constraints.

First, the extended topological derivative $D^{ij}J$ is defined using the conventional topological derivative $D_T^{ij}J$ as follows:

$$D^{ij}J = D_T^{ij}J - D_T^{ji}J, \tag{30}$$

where D_T^{ij} is the ratio of the variant of the objective function to the volume or area of the small region when a small region of radius $\varepsilon > 0$ with component j is inserted into the region with component i.

Next, we derive the topological derivatives of the assembly constraints for the optimization problem of a structure comprising two types of components i, j. Here, the objective function of the assembly constraint for components i and j is expressed as follows:

$$J_{ij} = F_i \cdot F_j \tag{31}$$

$$= \int_D \psi_j \chi_i \, d\Omega \cdot \int_D \psi_i \chi_j \, d\Omega. \tag{32}$$

As shown in Figure 12, we consider a small change in the above objective function J_{ij} when a small region Ω_ε, i.e., component j, is inserted into the region of component i. Here, the topological derivative $D_T^{ij}J$ for the assembly constraint is derived as follows:

$$D_T^{ij}J = \{\beta(1-\psi_i)\tilde{\psi}_i + \psi_i\} \int_D \psi_j \chi_i \, d\Omega + \{\beta(1-\psi_j)\tilde{\psi}_j - \psi_j\} \int_D \psi_i \chi_j \, d\Omega, \tag{33}$$

where $\tilde{\psi}_i$ is an adjoint variable obtained by solving the following adjoint equation:

$$-L^2 div(\boldsymbol{A}_i \cdot \nabla\tilde{\psi}_i) + L\boldsymbol{V}_i \cdot \nabla\tilde{\psi}_i + \beta\chi_i\tilde{\psi}_i = \chi_j. \tag{34}$$

Note that the obtained topological derivatives can be applied to both two- and three-dimensional cases. The corresponding derivation process is described in detail in the Appendix.

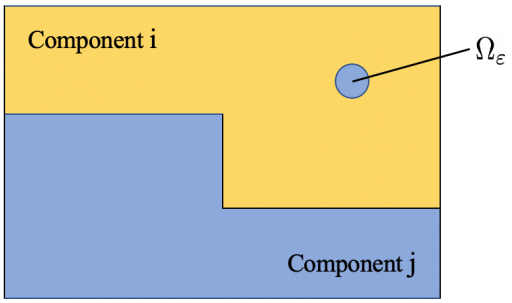

Figure 12: Insertion of small region Ω_ε.

5. Numerical implementation

Here, we describe a concrete numerical implementation method based on the formulations given in the previous sections.

5.1. Optimization algorithm

The optimization algorithm is summarized as follows.

Step 1 Give an appropriate initial value to the X-LS function ϕ_{ij}.

Step 2 Compute the displacement fields u, heat fields ψ, and adjoint fields $\tilde{\psi}$ using the finite element method.

Step 3 Evaluate the objective function and constraint function.

Step 4 If the objective function is converged, terminate the optimization calculation; otherwise, proceed to Step 5.

Step 5 Compute the extended topological derivative $D^{ij}J$.

Step 6 Calculate the reaction–diffusion equation using the finite element method and update the X-LS function. Return to Step 2.

In this study, the FreeFEM++ [43] finite element analysis software was used for finite element analysis.

5.2. Approximating the characteristic function

Note that condition (10) to be satisfied by the X-LS function is not completely satisfied by the optimization calculation, i.e., some regions cannot be assigned to any component. Thus, we define an approximate characteristic function $\hat{\chi}_m$ that approximates Equation (8) as follows:

$$\hat{\chi}_m = \prod_{i \neq m} H(\tilde{\phi}_{im}), \tag{35}$$

where $\tilde{\phi}_{ij}$ is an X-LS function whose zero isosurface in the approximated expression represents the boundary surface between components i and j. This function is defined as follows:

$$\tilde{\phi}_{im} = \tilde{\chi}_m - \tilde{\chi}_i \tag{36}$$

$$\tilde{\chi}_m = \prod_{i} \tilde{H}(\phi_{im}). \tag{37}$$

However, the $\tilde{\chi}_m$ function indicates the priority at which phase m is assigned at coordinate $\boldsymbol{x}$. Phase m with the largest $\tilde{\chi}_m$ is assigned to coordinate $\boldsymbol{x}$. Note that $\tilde{H}(s)$ is an approximated Heaviside function that

is defined as follows:

$$\tilde{H}(s) = \begin{cases} 0 & (s < -1) \\ \frac{1}{2} + s[\frac{15}{16} - s^2(\frac{5}{8} - \frac{3}{16}s^2)] & (-1 \leq s \leq 1) \\ 1 & (s > 1). \end{cases} \tag{38}$$

5.3. Sensitivity weighting

In the reaction–diffusion equation (Equation (11)), we can implement optimization that considers assemblability by adding the sensitivity $\tilde{J}'$ of the assembly constraint to the terms of the extended topological derivative $D^{ij}J$. Here, the strength of the assembly constraint can be changed by multiplying the sensitivity $\tilde{J}'$ of the assembly constraint by the weight factor γ as follows:

$$\frac{\partial \phi_{ij}}{\partial t} = -K(D^{ij}J + \gamma\,\tilde{J}' - \tau_{ij}\nabla^2\phi_{ij}). \tag{39}$$

The value of the weighting factor γ affects the optimal structure. For example, if weighting factor γ is too small, the constraint is not satisfied. In contrast, if it is too large, the solution tends to be local. Parameter γ is examined in detail in Section 6.

In the initial stage of the optimization calculation, if the assembly constraints are applied while the boundaries of each component domain are unclear, the optimization calculation tends to become unstable. Thus, in order to stabilize the calculation, the weight coefficient γ is set to 0 until the number of steps of the calculation where the boundary definition becomes clear.

6. Numerical examples

In the following, to verify the validity and effectiveness of the proposed method, we present several numerical examples for the multicomponent topology optimization problem with assemblability formulated in the previous section.

Here, up to four types of components (plus the cavity region) are considered for optimization. Each component is assumed to be an isotropic linear elastic material with a Young's modulus of $(E_1, E_2, E_3, E_4, E_{\text{void}}) = (100, 200, 400, 600, 0.1)$ GPa and a Poisson's ratio of $\gamma_m = 0.3$. The modulus E_{void} is used to represent the cavity by making it sufficiently small compared to the other components (ersatz material approach [18]). The following figures show the regions of component $1, 2, 3, 4$ in red, blue, green, and yellow, respectively, and the hollow regions are shown in gray.

6.1. Mean compliance minimization problem in two dimensions

Here, we apply the assembly constraints to the problem of minimizing the mean compliance of two components in a two-dimensional plane stress field. Figure 13 shows the design domain D and boundary conditions. In this case, the representative length L was set to 1.0, and the virtual time width Δt for the 1

step of the optimization was set to 0.1. In addition, the advection velocity V used in the steady advection–diffusion equation was set to 100, and the small constant ε used in the diffusion coefficient tensor $\boldsymbol{A}$ was set to 0.01. The weighting factor γ was set to 0 until the 5th step of calculation for stabilization, and from the 6th step, the predetermined value of the weighting factor was used.

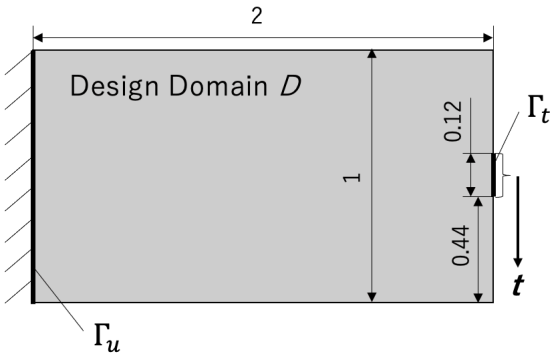

Figure 13: Two-dimensional problem settings for mean compliance minimization.

First, the optimization calculations were performed under the constraint that the first component (red) decomposes to the right and the second component (blue) decomposes to the left. Here, the regularization factor τ was set to 1.0×10^{-4} for all i, j, and the weight factor γ for the assembly constraint was set to 0.1. The maximum percentage of the volume of each component to the design area in the volume constraint was $(V_1, V_2, V_{\max}^{\text{void}}) = (25, 25, 100)\%$. In addition, the initial value of the X-LS function was set to $\phi_{ij} = 0$ for all i, j.

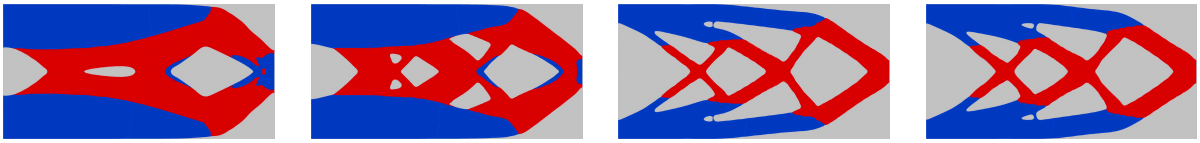

(a) Step 20. (b) Step 50. (c) Step 100. (d) Optimal configuration.

Figure 14: Intermediate results and optimal configuration with assembly constraints. The red and blue regions represent the first and second components, respectively.

Next, the optimization calculation was performed under the constraint that the decomposition directions of the two components are switched, i.e., the first component (red) decomposes to the left, and the second component (blue) decomposes to the right. Here, each parameter was set to value identified in the previous example.

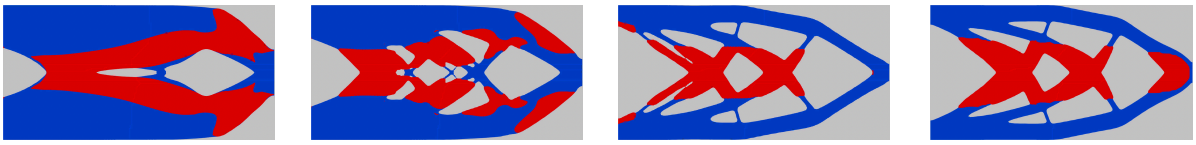

(a) Step 20. (b) Step 50. (c) Step 100. (d) Optimal configuration.

Figure 15: Intermediate results and optimal configuration with assembly constraints (assembly direction reversed). The red and blue regions represent the first and second components, respectively.

Finally, for comparison, the results of the optimization calculation for $\gamma = 0$, i.e., without assembly constraints, are shown in Figure 16.

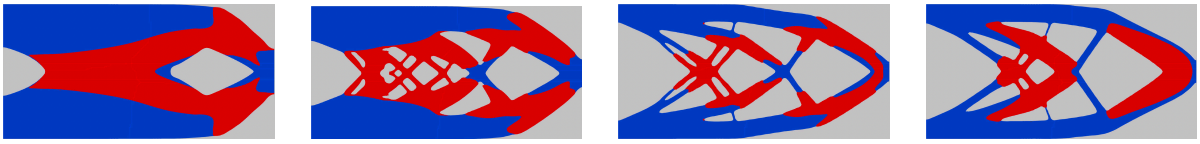

(a) Step 20. (b) Step 50. (c) Step 100. (d) Optimal configuration.

Figure 16: Intermediate results and optimal configuration without assembly constraints.

As can be seen, the boundary shapes obtained from the optimization calculations are clear and smooth, and the optimal structures are both structurally valid and clearly decomposable in the specified directions. In addition, by switching the decomposition directions, components with a high Young's modulus are preferentially placed where stresses are concentrated, which confirms that both assemblability and stiffness are optimized simultaneously. The mean compliance for each optimal configuration is 5.40×10^{-12} in Figure 14 and 5.14×10^{-12} in Figure 15, compared to 5.12×10^{-12} for the optimal configuration without assembly constraints. Thus, we conclude that the assembly constraint was achieved while maintaining a small mean compliance.

We also investigated the effect of the initial structure on the optimal configuration. Here, we performed the optimization calculations with different initial structures under the constraint that the first component (red) decomposes to the right and the second component (blue) decomposes to the left. The regularization factor τ_{ij} was set to 3.0×10^{-4} for all i, j, and the weight factor γ for the assembly constraint was set to 0.1. The maximum percentage of the volume of each component to the design area in the volume constraint was set to $(V_1, V_2, V_{\max}^{\text{void}}) = (25, 25, 100)\%$. The results are shown in Figure 20

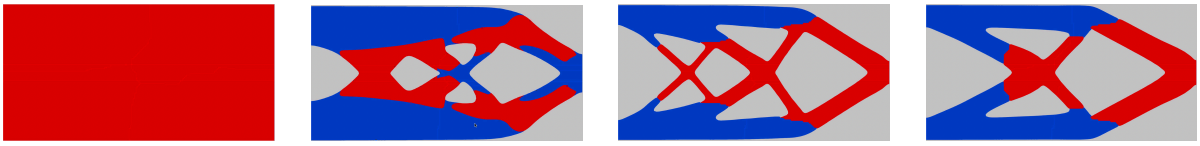

(a) Step 0. (b) Step 20. (c) Step 50. (d) Optimal configuration.

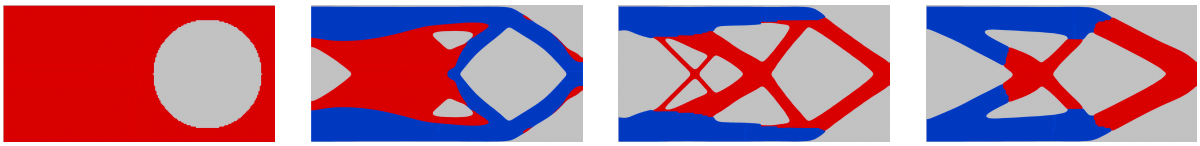

(a) Step 0. (b) Step 20. (c) Step 50. (d) Optimal configuration.

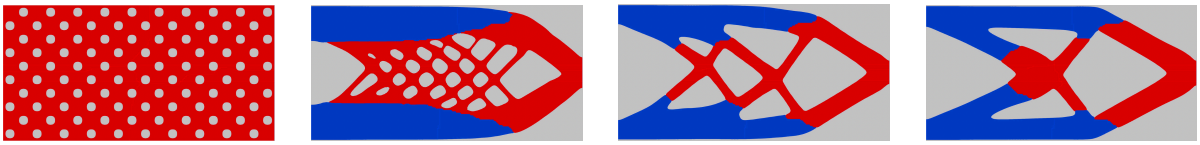

(a) Step 0. (b) Step 20. (c) Step 50. (d) Optimal configuration.

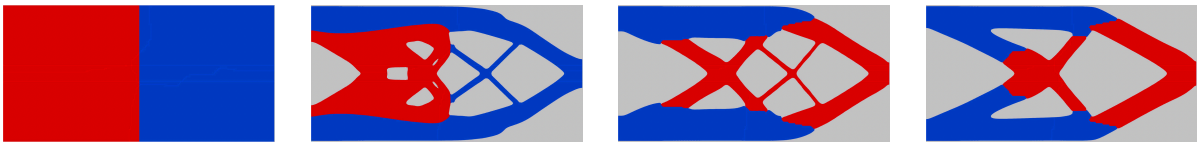

(a) Step 0. (b) Step 20. (c) Step 50. (d) Optimal configuration.

Figure 20: Intermediate results and optimal configuration with different initial structures.

As can be seen, the optimal structures obtained for the four different initial structures are nearly the same. Here, the mean compliance value was 5.63×10^{-12} for all of the optimal structures. In other words, appropriate optimal structures were obtained for all initial structures. Thus, these results confirm that the optimal structure obtained by the proposed method has little dependence on the initial structure.

In addition, the effect of the weight factor γ of the assembly constraint on the optimal structure was investigated. Here, under the constraint that the first component (red) decomposes to the left and the second component (blue) decomposes to the right, only the weight factor γ was varied without changing the other parameters. The results are shown in Figure 21 – 24. In this example, the regularization factor τ_{ij} was set to 5.0×10^{-4} for all i, j, the initial value of the X-LS function was set to $\phi_{ij} = 0$ for all i, j, and the maximum percentage of the volume of each component in the volume constraint to the design domain was set to $(V_1, V_2, V_{\max}^{\text{void}}) = (25, 25, 100)\%$. The weight coefficients were $\gamma = (0.001,\ 0.1,\ 10,\ 1000)$.

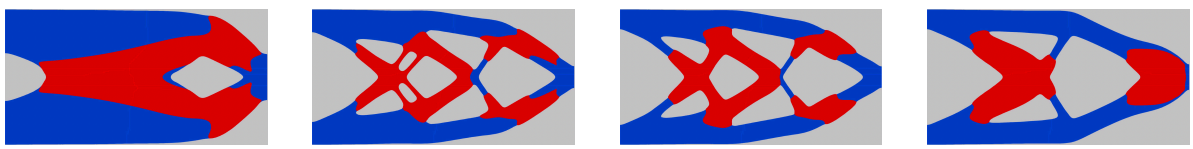

(a) Step 20. (b) Step 50. (c) Step 100. (d) Optimal configuration.

Figure 21: Intermediate results and optimal configuration for $\gamma = 0.001$.

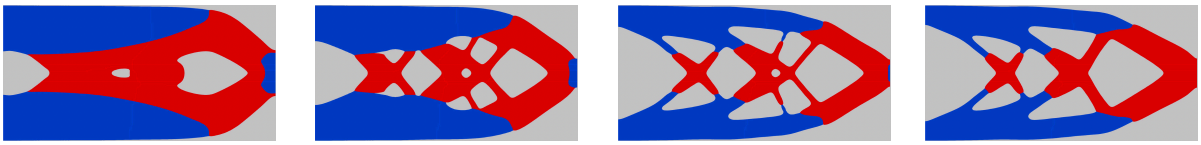

(a) Step 20. (b) Step 50. (c) Step 100. (d) Optimal configuration.

Figure 22: Intermediate results and optimal configuration for $\gamma = 0.1$.

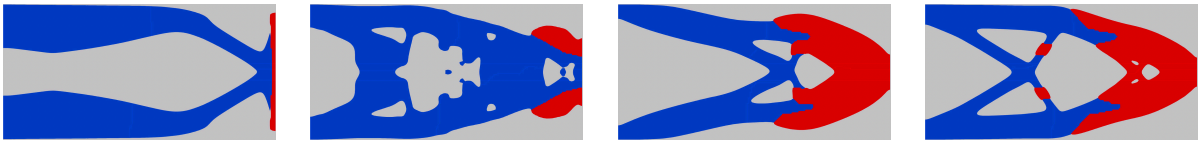

(a) Step 20. (b) Step 50. (c) Step 100. (d) Optimal configuration.

Figure 23: Intermediate results and optimal configuration for $\gamma = 10$.

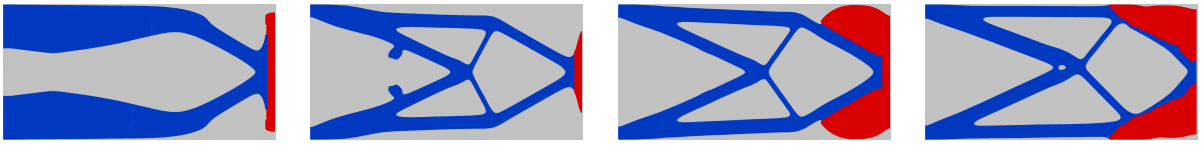

(a) Step 20. (b) Step 50. (c) Step 100. (d) Optimal configuration.

Figure 24: Intermediate results and optimal configuration for $\gamma = 1000$.

The mean compliance of each optimal structure is $(5.24 \times 10^{-12}, 5.33 \times 10^{-12}, 5.34 \times 10^{-12}, 6.73 \times 10^{-12})$ for $\gamma = (0.001, 0.1, 10, 1000)$, respectively. These results confirm that the assembly constraint is not satisfied if weight factor γ is too small. In contrast, if γ is too large, the assembly constraint is satisfied early; however, the solution tends to be local and less rigid.

6.2. Mean compliance minimization problem in three dimensions

To verify the practical applicability of the proposed method, it was applied to the optimal design problem of a three-dimensional mechanical component. Figure 25 shows the fixed design domain, the nondesign domain, and the boundary conditions. Here, the fixed design region is shown in gray, and the nondesign region is shown in blue. In this case, the representative length L was set to 0.2. Component 2 was assigned to the nondesign region. The initial value of the X-LS function was set to $\phi_{ij} = 0$, and the virtual time width for a single optimization step was $\Delta t = 0.1$. In addition, the advection velocity used in the steady advection–diffusion equation was $V = 10$, and the small constant used in the diffusion coefficient tensor $\boldsymbol{A}$ was $\varepsilon = 0.01$. The weight coefficient γ was set to 0 until the 10th step of calculation for stabilization, and a predetermined value was used from the 11th step.

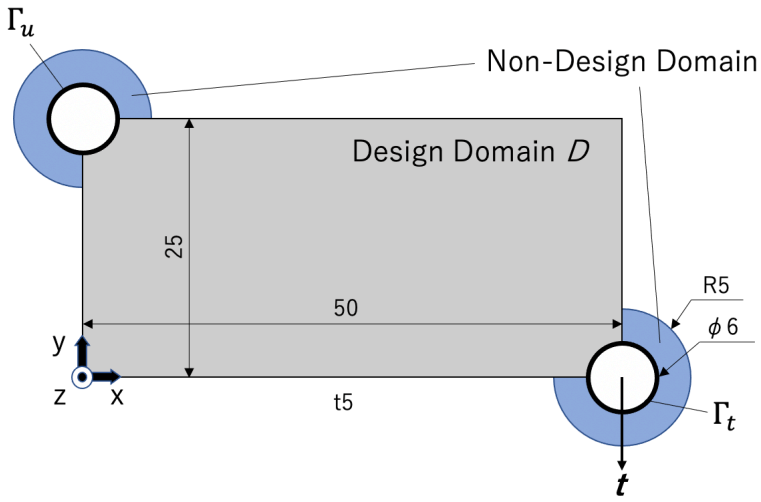

Figure 25: Three-dimensional problem settings.

First, for comparison, a numerical example of a three-dimensional model with four components without assembly constraints, i.e., $\gamma = 0$, is shown in Figure 26. Here, the regularization factor τ_{ij} was set to 1.0×10^{-3} for all i, j, and the maximum value of the ratio of the volume of each component to the design area in the volume constraint was $(V_1, V_2, V_3, V_4, V_{\max}^{\text{void}}) = (10, 10, 10, 10, 100)\%$.

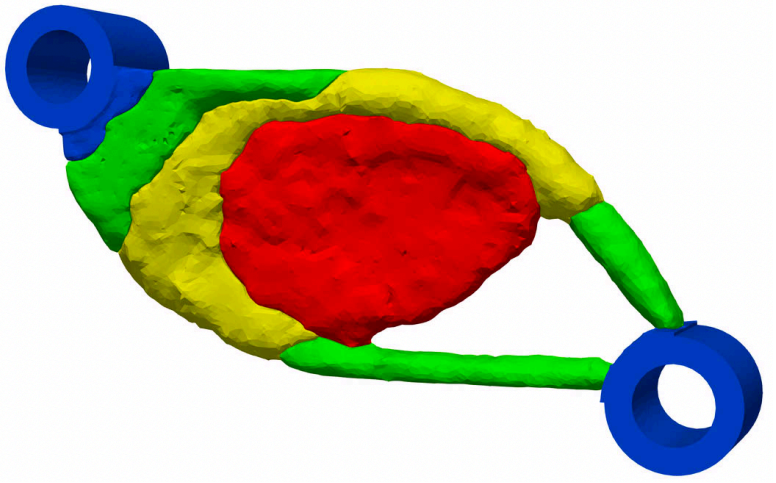

Figure 26: Optimal configuration in three dimensions with four components without assembly constraints.

The mean compliance in the optimal structure was 4.16×10^{-6}.

Next, we show the results of the numerical analysis when assembly constraints were applied. In this analysis, the weight factor of the assembly constraint was set to $\gamma = 10.0$, and the other parameters were the same as the case shown in Figure 26. To obtain a structure with better performance, the decomposition

direction should be set in a direction and order that are as natural as possible for the optimal structure obtained without assembly constraints. Thus, as an example, for Fig. 26, the optimization calculation was performed under the stepwise constraint that component 3 (green) decomposes to the left, component 4 (yellow) decomposes to the right, and then components 2 (blue) and 1 (red) are split into upper and lower parts. The results are shown in Figure 27.

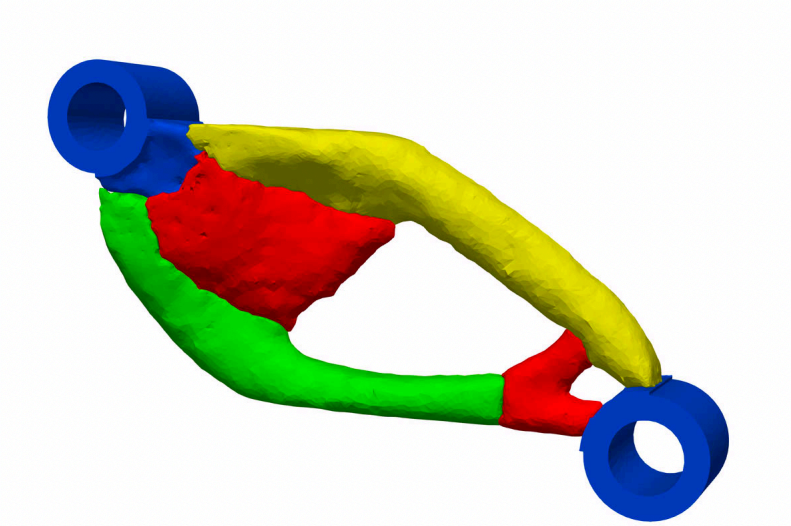

Figure 27: Optimal configuration in three dimensions with four components.

For the optimal structure, the mean compliance was found to be 4.44×10^{-6}. As shown in the Figures 28 and 29, the obtained optimal structure can be decomposed in the specified direction. In addition, the mean compliance does not increase significantly compared to the unconstrained case, and the structure is considered reasonable in terms of structural dynamics. Thus, these results confirm that the proposed method can realize the stepwise assembly constraint in three dimensions with four components.

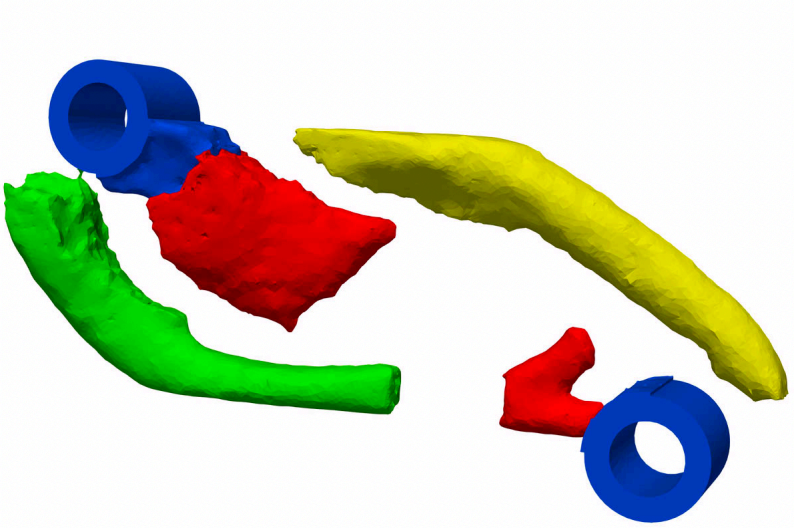

Figure 28: Stepwise decomposition steps 1 and 2.

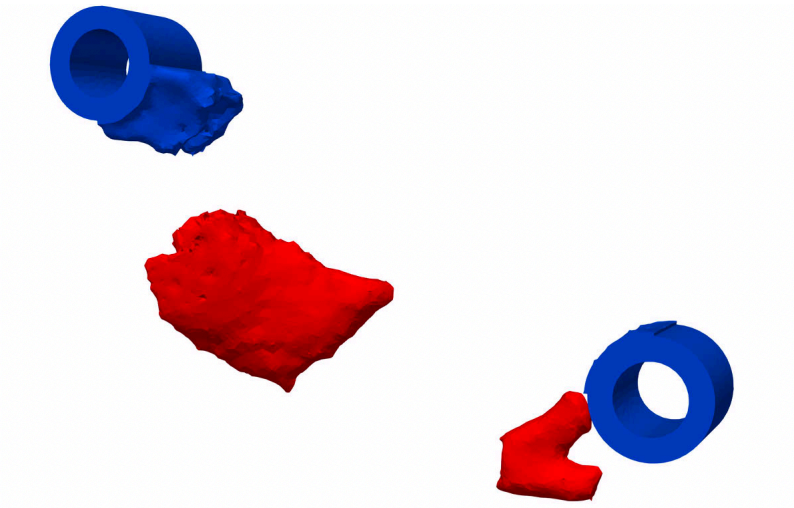

Figure 29: Stepwise decomposition step 3.

7. Concusion

In this paper, we have proposed a multicomponent topology optimization method that considers assemblability. The primary findings of this study are summarized as follows.

1. We have clarified the geometric requirements in assembly constraints, i.e., excluding undercut and interior void shapes.
2. The assembly constraints for two components were formulated using a fictitious heat field.
3. By considering assembly in stages, we extended the assembly constraints to more than three components.
4. A concrete numerical analysis algorithm for a topology optimization method considering assembly constraints was constructed.
5. Numerical analysis of two-dimensional design problems was performed to verify the proposed method.
   - We obtained a structure with assemblability in a predefined direction.
   - We have demonstrated that, even if the assembly directions are switched, optimization can be realized by considering the properties of the component.
   - We confirmed that the topology optimization by the proposed method has a low initial structure dependence.
   - The influence of the weight coefficient γ of the assembly constraint on the optimal structure was investigated: if γ is too small, the assembly constraint is not satisfied, and if γ is too large, the solution tends to be local and less rigid.
6. Through numerical examples, we have demonstrated that the proposed method can be applied to three-dimensional design problems: we obtained a structure with predefined directional assemblability without significantly reducing rigidity.

Potential future work is summarized as follows.

1. The proposed method's applicability to optimization problems involving other physical fields, e.g., heat transfer, vibration, electromagnetic, acoustic, and fluid flow problems, should be verified.
2. The assembly direction of each component can also be optimized further.
3. Optimization considering stress at the boundary should be investigated further.

Acknowledgments

This work was supported in part by JSPS KAKENHI Grant Number 19H02049.

Appendix A. Derivation of topological derivatives

Here, consider a situation where a small region Ω_ε, i.e., component j, is inserted into the region of component i, as shown in Figure 12. In this case, the governing equation for $\forall\tilde{\psi_m} \in H^1(\Omega)$ $(m = i, j)$ is expressed as follows:

$$a_\varepsilon(\psi_m^\varepsilon, \tilde{\psi_m}) = l_\varepsilon(\tilde{\psi_m}) \qquad \forall\tilde{\psi_m} \in H^1(\Omega), \tag{A.1}$$

where $a_\varepsilon(\psi_m^\varepsilon, \tilde{\psi_m})$, and $l_\varepsilon(\tilde{\psi_m})$ are expressed as follows:

$$\begin{aligned} a_\varepsilon(\psi_m^\varepsilon, \tilde{\psi_m}) &= \int_D L^2\nabla\tilde{\psi_m}\cdot(\boldsymbol{A}\nabla\psi_m^\varepsilon)\,d\Omega + \int_D L(\boldsymbol{V}\cdot\nabla\psi_m^\varepsilon)\tilde{\psi_m}\,d\Omega \\ &+ \int_D \beta\chi_m\psi_m^\varepsilon\tilde{\psi_m}\,d\Omega \end{aligned} \tag{A.2}$$

$$l_\varepsilon(\tilde{\psi_m}) = \begin{cases} \int_{\Omega_i\setminus\Omega_\varepsilon} \beta\tilde{\psi_i}\,d\Omega & (m = i) \\ \int_{\Omega_j\cup\Omega_\varepsilon} \beta\tilde{\psi_j}\,d\Omega & (m = j). \end{cases} \tag{A.3}$$

Note that the following equation should be satisfied before Ω_ε appears.

$$a_0(\psi_m, \tilde{\psi_m}) = l_0(\tilde{\psi_m}) \qquad \forall\tilde{\psi_m} \in H^1(\Omega), \tag{A.4}$$

where $a_0(\psi_m, \tilde{\psi_m})$, and $l_0(\tilde{\psi_m})$ are expressed as follows:

$$\begin{aligned} a_0(\psi_m, \tilde{\psi_m}) &= \int_D L^2\nabla\tilde{\psi_m}\cdot(\boldsymbol{A}\nabla\psi_m)\,d\Omega + \int_D L(\boldsymbol{V}\cdot\nabla\psi_m)\tilde{\psi_m}\,d\Omega \\ &+ \int_D \beta\chi_m\psi_m\tilde{\psi_m}\,d\Omega \end{aligned} \tag{A.5}$$

$$l_0(\tilde{\psi_m}) = \int_{\Omega_m} \beta\tilde{\psi_m}\,d\Omega. \tag{A.6}$$

At this time, the small change δJ_{ij} in the objective function J_{ij} defined in Equation (31) is expressed as follows:

$$\begin{aligned} \delta J_{ij} &= J_{ij}^\varepsilon - J_{ij} \\ &= F_i^\varepsilon\cdot F_j^\varepsilon - F_i\cdot F_j \\ &= (F_i + \delta F_i^\varepsilon)(F_j + \delta F_j^\varepsilon) - F_i\cdot F_j \\ &\simeq \delta F_j^\varepsilon\cdot F_i + \delta F_i^\varepsilon\cdot F_j, \end{aligned} \tag{A.7}$$

where δF_i^ε is the small change in the objective function F_i, which is defined as follows:

$$\begin{aligned}
\delta F_i^\varepsilon &= F_i^\varepsilon - F_i \\
&= \{F_i^\varepsilon - a_\varepsilon(\psi_j^\varepsilon,\, \tilde{\psi_j}) + l_\varepsilon(\tilde{\psi_j})\} - \{F_i - a_0(\psi_j,\, \tilde{\psi_j}) + l_0(\tilde{\psi_j})\} \\
&= \int_{\Omega_i \setminus \Omega_\varepsilon} \psi_j^\varepsilon \, d\Omega - \int_{\Omega_i} \psi_j \, d\Omega \\
&- a_\varepsilon(\psi_j^\varepsilon,\, \tilde{\psi_j}) + a_0(\psi_j,\, \tilde{\psi_j}) + l_\varepsilon(\tilde{\psi_j}) - l_0(\tilde{\psi_j}) \\
&= \int_{\Omega_i \setminus \Omega_\varepsilon} (\psi_j^\varepsilon - \psi_j) \, d\Omega + \int_{\Omega_i \setminus \Omega_\varepsilon} \psi_j \, d\Omega - \int_{\Omega_i} \psi_j \, d\Omega \\
&- a_\varepsilon(\psi_j^\varepsilon,\, \tilde{\psi_j}) + a_0(\psi_j,\, \tilde{\psi_j}) + l_\varepsilon(\tilde{\psi_j}) - l_0(\tilde{\psi_j}) \\
&= \int_{\Omega_i \setminus \Omega_\varepsilon} (\psi_j^\varepsilon - \psi_j) \, d\Omega - \int_{\Omega_\varepsilon} \psi_j \, d\Omega \\
&- a_\varepsilon(\psi_j^\varepsilon - \psi_j,\, \tilde{\psi_j}) - (a_\varepsilon - a_0)(\psi_j,\, \tilde{\psi_j}) + (l_\varepsilon - l_0)(\tilde{\psi_j}). \qquad \text{(A.8)}
\end{aligned}$$

Here, $(a_\varepsilon - a_0)(\psi_j,\, \tilde{\psi_j})$, and $(l_\varepsilon - l_0)(\tilde{\psi_j})$ are expressed as follows:

$$\begin{aligned}
(a_\varepsilon - a_0)(\psi_j,\, \tilde{\psi_j}) &= \int_{\Omega_\varepsilon} \beta \psi_j \tilde{\psi_j} \, d\Omega \\
(l_\varepsilon - l_0)(\tilde{\psi_j}) &= \int_{\Omega_\varepsilon} \beta \tilde{\psi_j} \, d\Omega. \qquad \text{(A.9)}
\end{aligned}$$

Using the solution $\tilde{\psi_j^\varepsilon}$ obtained by solving the adjoint equation as expressed below, we can cancel the first and third terms on the right-hand side of Equation (A.8) and avoid evaluating the heat field ψ_j^ε.

$$\int_D L^2 \nabla\eta \cdot (\boldsymbol{A} \nabla \tilde{\psi_j^\varepsilon}) \, d\Omega + \int_D L(\boldsymbol{V} \cdot \nabla \tilde{\psi_j^\varepsilon}) \eta \, d\Omega + \int_D \beta \chi_j \tilde{\psi_j^\varepsilon} \eta \, d\Omega = \int_{\Omega_i \setminus \Omega_\varepsilon} \eta \, d\Omega. \qquad \text{(A.10)}$$

In this case, Equation (A.8) is expressed using the adjoint field $\tilde{\psi_j^\varepsilon}$ as follows:

$$\begin{aligned}
\delta F_i^\varepsilon &= \int_{\Omega_\varepsilon} \beta \tilde{\psi_j}^{\,\varepsilon} \, d\Omega - \int_{\Omega_\varepsilon} \beta \psi_j \tilde{\psi_j^\varepsilon} \, d\Omega - \int_{\Omega_\varepsilon} \psi_j \, d\Omega \\
&= \int_{\Omega_\varepsilon} \beta(1 - \psi_j) \tilde{\psi_j^\varepsilon} \, d\Omega - \int_{\Omega_\varepsilon} \psi_j \, d\Omega \qquad \text{(A.11)}
\end{aligned}$$

Similarly, the small change δF_j^ε of the objective function F_j can be obtained as follows:

$$\delta F_j^\varepsilon = \int_{\Omega_\varepsilon} \beta(1 - \psi_i) \tilde{\psi_i^\varepsilon} \, d\Omega + \int_{\Omega_\varepsilon} \psi_i \, d\Omega, \qquad \text{(A.12)}$$

where $\tilde{\psi_i^\varepsilon}$ is the solution to the following adjoint equation:

$$\int_D L^2 \nabla\eta \cdot (\boldsymbol{A} \nabla \tilde{\psi_i^\varepsilon}) \, d\Omega + \int_D L(\boldsymbol{V} \cdot \nabla \tilde{\psi_i^\varepsilon}) \eta \, d\Omega + \int_D \beta \chi_i \tilde{\psi_i^\varepsilon} \eta \, d\Omega = \int_{\Omega_j \cup \Omega_\varepsilon} \eta \, d\Omega. \qquad \text{(A.13)}$$

Thus, Equation (A.7) can be expressed as follows:

$$\begin{aligned}
\delta J_{ij} &= \left\{\int_{\Omega_\varepsilon} \beta(1-\psi_i)\tilde{\psi}_i^\varepsilon \, d\Omega + \int_{\Omega_\varepsilon} \psi_i \, d\Omega\right\} \cdot F_i + \left\{\int_{\Omega_\varepsilon} \beta(1-\psi_j)\tilde{\psi}_j^\varepsilon \, d\Omega - \int_{\Omega_\varepsilon} \psi_j \, d\Omega\right\} \cdot F_j \\
&\simeq \left\{\int_{\Omega_\varepsilon} \beta(1-\psi_i)\tilde{\psi}_i \, d\Omega + \int_{\Omega_\varepsilon} \psi_i \, d\Omega\right\} \cdot F_i + \left\{\int_{\Omega_\varepsilon} \beta(1-\psi_j)\tilde{\psi}_j \, d\Omega - \int_{\Omega_\varepsilon} \psi_j \, d\Omega\right\} \cdot F_j \\
&\simeq |\Omega_\varepsilon| \left\{\beta(1-\psi_i)\tilde{\psi}_i + \psi_i\right\} \int_D \psi_j \chi_i \, d\Omega + |\Omega_\varepsilon| \left\{\beta(1-\psi_j)\tilde{\psi}_j - \psi_j\right\} \int_D \psi_i \chi_j \, d\Omega \\
&\simeq (\pi\varepsilon^2)\{\beta(1-\psi_i)\tilde{\psi}_i + \psi_i\} \int_D \psi_j \chi_i \, d\Omega + (\pi\varepsilon^2)\{\beta(1-\psi_j)\tilde{\psi}_j - \psi_j\} \int_D \psi_i \chi_j \, d\Omega.
\end{aligned} \tag{A.14}$$

Therefore, the topological derivative $D_T^{ij} J$ can be expressed as follows:

$$\begin{aligned}
D_T^{ij} J &= \lim_{\varepsilon \to 0} \frac{\delta J_{ij}}{\pi\varepsilon^2} \\
&= \{\beta(1-\psi_i)\tilde{\psi}_i + \psi_i\} \int_D \psi_j \chi_i \, d\Omega + \{\beta(1-\psi_j)\tilde{\psi}_j - \psi_j\} \int_D \psi_i \chi_j \, d\Omega.
\end{aligned} \tag{A.15}$$

Competing interests

The authors declare no conflicts of interest.

Author contributions statement

R.H. conducted the numerical simulations and wrote the manuscript. M.N., K.M, and Y.N. analyzed the results. T.Y. supervised the project.

References

[1] M. P. Bendsøe, N. Kikuchi, Generating optimal topologies in structural design using a homogenization method, Computer Methods in Applied Mechanics and Engineering 71 (2) (1988) 197–224. doi:10.1016/0045-7825(88)90086-2.

[2] M. P. Bendsøe, Optimal shape design as a material distribution problem, Structural optimization 1 (4) (1989) 193–202. doi:10.1007/BF01650949.

[3] M. P. Bendsøe, O. Sigmund, Material interpolation schemes in topology optimization, Archive of Applied Mechanics 69 (9) (1999) 635–654. doi:10.1007/s004190050248.

[4] G. Allaire, Shape Optimization by the Homogenization Method, Springer, 2002.

[5] K. Suzuki, N. Kikuchi, A homogenization method for shape and topology optimization, Computer Methods in Applied Mechanics and Engineering 93 (3) (1991) 291–318. doi:10.1016/0045-7825(91)90245-2.

[6] J. A. Sethian, A. Wiegmann, Structural boundary design via level set and immersed interface methods, Journal of Computational Physics 163 (2) (2000) 489–528. doi:10.1006/jcph.2000.6581.

[7] G. Allaire, F. de Gournay, F. Jouve, A.-M. Toader, Structural optimization using topological and shape sensitivity via a level set method, Control and Cybernetics 34 (1) (2005) 59–80.

[8] T. Yamada, K. Izui, S. Nishiwaki, A. Takezawa, A topology optimization method based on the level set method incorporating a fictitious interface energy, Computer Methods in Applied Mechanics and Engineering 199 (45) (2010) 2876–2891. doi:10.1016/j.cma.2010.05.013.

[9] S. Amstutz, H. Andrä, A new algorithm for topology optimization using a level-set method, Journal of Computational Physics 216 (2) (2006) 573–588. doi:10.1016/j.jcp.2005.12.015.

[10] A. R. Díaaz, N. Kikuchi, Solutions to shape and topology eigenvalue optimization problems using a homogenization method, International Journal for Numerical Methods in Engineering 35 (7) (1992) 1487–1502. doi:10.1002/nme.1620350707.

[11] Z.-D. Ma, N. Kikuchi, H.-C. Cheng, Topological design for vibrating structures, Computer Methods in Applied Mechanics and Engineering 121 (1) (1995) 259–280. doi:10.1016/0045-7825(94)00714-X.

[12] A. Gersborg-Hansen, M. P. Bendsøe, O. Sigmund, Topology optimization of heat conduction problems using the finite volume method, Structural and Multidisciplinary Optimization 31 (4) (2006) 251–259. doi:10.1007/s00158-005-0584-3.

[13] T. Yamada, K. Izui, S. Nishiwaki, A level set-based topology optimization method for maximizing thermal diffusivity in problems including design-dependent effects, Journal of Mechanical Design 133 (3) (2011) 031011. doi:10.1115/1.4003684.

[14] G. Jing, H. Isakari, T. Matsumoto, T. Yamada, T. Takahashi, Level set-based topology optimization for 2D heat conduction problems using BEM with objective function defined on design-dependent boundary with heat transfer boundary condition, Engineering Analysis with Boundary Elements 61 (2015) 61–70. doi:10.1016/j.enganabound.2015.06.012.

[15] J. Yoo, N. Kikuchi, J. Volakis, Structural optimization in magnetic devices by the homogenization design method, IEEE Transactions on Magnetics 36 (3) (2000) 574–580. doi:10.1109/20.846220.

[16] T. Yamada, H. Watanabe, G. Fujii, T. Matsumoto, Topology optimization for a dielectric optical cloak based on an exact level set approach, IEEE Transactions on Magnetics 49 (5) (2013) 2073–2076. doi:10.1109/TMAG.2013.2243120.

[17] J. Du, N. Olhoff, Minimization of sound radiation from vibrating bi-material structures using topology optimization, Structural and Multidisciplinary Optimization 33 (4) (2007) 305–321. doi:10.1007/s00158-006-0088-9.

[18] Y. Noguchi, T. Yamada, Level set-based topology optimization for graded acoustic metasurfaces using two-scale homogenization, Finite Elements in Analysis and Design 196 (2021) 103606. doi:10.1016/j.finel.2021.103606.

[19] L. Wang, P. K. Basu, J. P. Leiva, Automobile body reinforcement by finite element optimization, Finite Elements in Analysis and Design 40 (8) (2004) 879–893. doi:10.1016/S0168-874X(03)00118-5.

[20] W. Saleem, F. Yuqing, W. Yunqiao, Application of topology optimization and manufacturing simulations - a new trend in design of aircraft components, Proceedings of the International MultiConference of Engineers and Computer Scientists 2.

[21] T. Yamada, K. Izui, S. Nishiwaki, M. Sato, O. Tabata, An optimal structural design method for capacitive ultrasonic transducers: Topology optimization with uniform cross-section surface constraint based on the level set method (in Japanese), Transactions of the JSME, Series A 76 (771) (2010) 1403–1411.

[22] S. Liu, Q. Li, W. Chen, L. Tong, G. Cheng, An identification method for enclosed voids restriction in manufacturability design for additive manufacturing structures, Frontiers of Mechanical Engineering 10 (2) (2015) 126–137. doi:10.1007/s11465-015-0340-3.

[23] Q. Li, W. Chen, S. Liu, L. Tong, Structural topology optimization considering connectivity constraint, Structural and Multidisciplinary Optimization 54 (4) (2016) 971–984. doi:10.1007/s00158-016-1459-5.

[24] L. Zhou, W. Zhang, Topology optimization method with elimination of enclosed voids, Structural and Multidisciplinary Optimization 60 (1) (2019) 117–136. doi:10.1007/s00158-019-02204-y.

[25] Y. Zhou, T. Nomura, K. Saitou, Multicomponent topology optimization for additive manufacturing with build volume and cavity free constraints, Journal of Computing and Information Science in Engineering 19 (2) (2019) 021011. doi:10.1115/1.4042640.

[26] Y. Zhou, T. Nomura, K. Saitou, Anisotropic multicomponent topology optimization for additive manufacturing with build

orientation design and stress-constrained interfaces, Journal of Computing and Information Science in Engineering 21 (1) (2020) 011007. doi:10.1115/1.4047487.

[27] C. Wang, Simultaneous optimization of build orientation and topology for self-supported enclosed voids in additive manufacturing, Computer Methods in Applied Mechanics and Engineering 388 (2022) 114227. doi:10.1016/j.cma.2021.114227.

[28] L. Crispo, I. Y. Kim, Part consolidation for additive manufacturing: A multilayered topology optimization approach, International Journal for Numerical Methods in Engineering 122 (18) (2021) 4987–5027. doi:10.1002/nme.6754.

[29] L. Luo, I. Baran, S. Rusinkiewicz, W. Matusik, Chopper: Partitioning models into 3D-printable parts, ACM Transactions on Graphics 31 (6) (2012) 129:1–129:9. doi:10.1145/2366145.2366148.

[30] M. Attene, Shapes in a box: Disassembling 3D objects for efficient packing and fabrication, Computer Graphics Forum 34 (8) (2015) 64–76. doi:10.1111/cgf.12608.

[31] Z. Zhou, K. Hamza, K. Saitou, Decomposition templates and joint morphing operators for genetic algorithm optimization of multicomponent structural topology, Journal of Mechanical Design 136 (2) (2013) 021004. doi:10.1115/1.4026030.

[32] D. Guirguis, K. Hamza, M. Aly, H. Hegazi, K. Saitou, Multi-objective topology optimization of multi-component continuum structures via a Kriging-interpolated level set approach, Structural and Multidisciplinary Optimization 51 (3) (2015) 733–748. doi:10.1007/s00158-014-1154-3.

[33] Y. Oh, C. Zhou, S. Behdad, Part decomposition and assembly-based (Re) design for additive manufacturing: A review, Additive Manufacturing 22 (2018) 230–242. doi:10.1016/j.addma.2018.04.018.

[34] Y. Oh, C. Zhou, S. Behdad, Part decomposition and 2D batch placement in single-machine additive manufacturing systems, Journal of Manufacturing Systems 48 (2018) 131–139. doi:10.1016/j.jmsy.2018.07.006.

[35] Y. Oh, H. Ko, T. Sprock, W. Z. Bernstein, S. Kwon, Part decomposition and evaluation based on standard design guidelines for additive manufacturability and assemblability, Additive Manufacturing 37 (2021) 101702. doi:10.1016/j.addma.2020.101702.

[36] Z. Wang, P. Song, M. Pauly, State of the art on computational design of assemblies with rigid parts, Computer Graphics Forum 40 (2) (2021) 633–657. doi:10.1111/cgf.142660.

[37] O. Sigmund, S. Torquato, Design of materials with extreme thermal expansion using a three-phase topology optimization method, Journal of the Mechanics and Physics of Solids 45 (6) (1997) 1037–1067. doi:10.1016/S0022-5096(96)00114-7.

[38] Y. Wang, Z. Luo, Z. Kang, N. Zhang, A multi-material level set-based topology and shape optimization method, Computer Methods in Applied Mechanics and Engineering 283 (2015) 1570–1586. doi:10.1016/j.cma.2014.11.002.

[39] P. Gangl, A multi-material topology optimization algorithm based on the topological derivative, Computer Methods in Applied Mechanics and Engineering 366 (2020) 113090. doi:10.1016/j.cma.2020.113090.

[40] M. Noda, Y. Noguchi, T. Yamada, Extended level set method: A multiphase representation with perfect symmetric property, and its application to multi-material topology optimization, Computer Methods in Applied Mechanics and Engineering 393 (2022) 114742. doi:10.1016/j.cma.2022.114742.

[41] T. Yamada, Y. Noguchi, Topology optimization with a closed cavity exclusion constraint for additive manufacturing based on the fictitious physical model approach, Additive Manufacturing 52 (2022) 102630. doi:10.1016/j.addma.2022.102630.

[42] Y. Sato, T. Yamada, K. Izui, S. Nishiwaki, Manufacturability evaluation for molded parts using fictitious physical models, and its application in topology optimization, The International Journal of Advanced Manufacturing Technology 92 (1) (2017) 1391–1409. doi:10.1007/s00170-017-0218-0.

[43] F. Hecht, New development in freefem++, Journal of Numerical Mathematics 20 (3-4) (2012) 251–266. doi:10.1515/jnum-2012-0013.